



HAL
open science

Arp2/3 Controls the Motile Behavior of N-WASP-Functionalized GUVs and Modulates N-WASP Surface Distribution by Mediating Transient Links with Actin Filaments

Vincent Delatour, Emmanuèle Helfer, Dominique Didry, Kim Ho Diep Le, Jean-François Gaucher, Marie-France Carlier, Guillaume Romet - Lemonne

► To cite this version:

Vincent Delatour, Emmanuèle Helfer, Dominique Didry, Kim Ho Diep Le, Jean-François Gaucher, et al.. Arp2/3 Controls the Motile Behavior of N-WASP-Functionalized GUVs and Modulates N-WASP Surface Distribution by Mediating Transient Links with Actin Filaments. *Biophysical Journal*, 2008, 94 (12), pp.4890-4905. 10.1529/biophysj.107.118653 . hal-01960884

HAL Id: hal-01960884

<https://hal.science/hal-01960884>

Submitted on 15 Jan 2024

HAL is a multi-disciplinary open access archive for the deposit and dissemination of scientific research documents, whether they are published or not. The documents may come from teaching and research institutions in France or abroad, or from public or private research centers.

L'archive ouverte pluridisciplinaire **HAL**, est destinée au dépôt et à la diffusion de documents scientifiques de niveau recherche, publiés ou non, émanant des établissements d'enseignement et de recherche français ou étrangers, des laboratoires publics ou privés.

Arp2/3 Controls the Motile Behavior of N-WASP-Functionalized GUVs and Modulates N-WASP Surface Distribution by Mediating Transient Links with Actin Filaments

Vincent Delatour,^{*} Emmanuèle Helfer,^{*} Dominique Didry,^{*} Kim Hô Diệp Lê,^{*} Jean-François Gaucher,[†] Marie-France Carlier,^{*} and Guillaume Romet-Lemonne^{*}

^{*}Cytoskeleton Dynamics and Motility, Laboratoire d'Enzymologie et Biochimie Structurales, Centre National de la Recherche Scientifique, Gif-sur-Yvette, France; and [†]Laboratoire de Cristallographie et RMN Biologiques, Université Paris Descartes/Centre National de la Recherche Scientifique (UMR 8015) Faculté de Pharmacie, Paris, France

ABSTRACT Spatially controlled assembly of actin in branched filaments generates cell protrusions or the propulsion of intracellular vesicles and pathogens. The propulsive movement of giant unilamellar vesicles (GUVs) functionalized by N-WASP (full-length or truncated) is reconstituted in a biochemically controlled medium, and analyzed using phase contrast and fluorescence microscopy to elucidate the links between membrane components and the actin cytoskeleton that determine motile behavior. Actin-based propulsion displays a continuous regime or a periodic saltatory regime. The transition between the two regimes is controlled by the concentration of Arp2/3 complex, which branches filaments by interacting with N-WASP at the liposome surface. Saltatory motion is linked to cycles in the distribution of N-WASP at the membrane between a homogeneous and a segregated state. Comparison of the changes in distribution of N-WASP, Arp2/3, and actin during propulsion demonstrates that actin filaments bind to N-WASP, and that these bonds are transitory. This interaction, mediated by Arp2/3, drives N-WASP segregation. VC-fragments of N-WASP, that interact more weakly than N-WASP with the Arp2/3 complex, segregate less than N-WASP at the rear of the GUVs. GUV propulsion is inhibited by the presence of VCA-actin covalent complex, showing that the release of actin from the nucleator is required for movement. The balance between segregation and free diffusion determines whether continuous movement can be sustained. Computed surface distributions of N-WASP, derived from a theoretical description of this segregation-diffusion mechanism, account satisfactorily for the measured density profiles of N-WASP, Arp2/3 complex, and actin.

INTRODUCTION

The movements and changes in shape of living cells are elicited by the polarized growth of actin filaments that causes deformation of the membrane and the formation of protrusions (1–4). It is well accepted that the interplay of membrane and cytoskeleton dynamics is at the origin of actin-based motile processes, because signal-controlled protein machineries located at the plasma membrane are responsible for the nucleation and regulated growth of filaments. One of the most studied machineries is the family of WASP/WAVE proteins, activated at the plasma membrane by small GTPases of the Rho family, which use the Arp2/3 complex to generate a dendritic array of branched filaments responsible for the extension of lamellipodia (5,6). The same actin-based process, carried out by the same cell components, promotes intracellular propulsion of endocytic vesicles and pathogens or vesicle scission in macropinocytosis.

The reconstitution of actin-based movement *in vitro* with five proteins that were confirmed to be essential for lamellipodium extension has proven useful to test the concepts at the origin of motility, to measure the force produced by actin polymerization and, by challenging the role of specific com-

ponents, to gain insight into the link between molecular processes and movement at the mesoscopic scale (7–11). Insertional barbed end growth of filaments continuously created by branching is fed by treadmilling and arrested by capping (11). However, because the molecular details of the elementary steps involved in filament branching are not fully elucidated and some remain controversial, several molecular models have been proposed and debated (see (12), for review).

One model proposed that the Arp2/3 complex, activated at the membrane, dissociates from the membrane and binds to the side of existing filaments, initiating a lateral branch (6,13). The insertional growth of the barbed ends develops protrusion. In this model, the filaments are never attached to the membrane.

On the other hand, evidence showed that the actin filament meshwork is attached to propelling *Listeria* (14) and that Arp2/3 is incorporated in the actin tail upon branching at the surface of propelling N-WASP-coated beads, at the same rate as filaments grow (11). Interestingly, fluorescence speckle microscopy analysis of the dynamics of actin and Arp2/3 complex in the lamellipodial branched filament array of migrating *Drosophila* S2 cells also show that like in the biomimetic system, Arp2/3 is incorporated into the network at the cell edge and undergoes treadmilling-driven retrograde flow at the same rate of 2.44 $\mu\text{m}/\text{min}$ as actin speckles (15). Although both *in vitro* and *in vivo* observations support the

view that filament barbed end branching and growth occur at the same rate at the membrane-filament barbed end interface, the biochemical and structural details of the underlying molecular mechanism are not fully understood. The catalytically active VCA domain of N-WASP comprises a WH2 domain (V, for verprolin-homology) that binds a G-actin molecule, while the connector (C) region and the acidic (A) region together bind Arp2/3 complex. Polymerization assays in bulk solution show that neither VC nor CA fragments support branched filament formation. Filament branching requires the binding of the ternary complex of VCA with G-actin and Arp2/3 to a filament (13). A recent report by Co et al. (16) showed that when the isolated WH2 domain was presented at the surface of lipid-coated beads, the WH2-actin moiety associated with filament barbed ends independently of Arp2/3 complex. How the association and dissociation of WH2-actin and CA-Arp2/3 may occur during filament branching and growth is not known, but has bearings in motile behavior at the mesoscopic scale. The idea of a transient attachment of membrane-bound N-WASP to a filament led to the tethered ratchet model (17), in which attached filaments pull and free filaments grow and push.

In contrast with the transient attachment model, a third model of permanent attachment, or end-tracking model, also called “actoclampin” (18,19), assumes that N-WASP (or ActA + VASP in the *Listeria* case) makes an ATP-dependent clamp that is permanently attached to the growing filament like a stepping motor.

In the cellular context, actin polymerizes against the deformable plasma membrane. Here, N-WASP is in a fluid environment and its diffusion within the lipid bilayer may be hampered by transient or permanent attachment to a filament (20). The ability of N-WASP to diffuse freely or to be maintained in clusters in the membrane may also affect the morphogenesis of the actin meshwork. Finally, the mechanical and rheological properties of the membrane may impose a reaction to the force developed by actin polymerization, and thus regulate motility. The simple actin-based motility assay that consists of solid microspheres functionalized with N-WASP at fixed positions and propelling in a reconstituted medium of pure proteins (11) is not appropriate to provide insight into these issues, and soft, fluid objects such as functionalized vesicles (21–24) or droplets (25,26) can be used instead.

These issues are addressed here by analyzing reconstituted actin-based propulsion of giant unilamellar vesicles (GUVs) in controlled biochemical conditions. We show that the concentration of Arp2/3 complex controls a transition in the regime of propulsion from continuous to saltatory type. Changes in the distribution of N-WASP at the surface of GUVs during saltatory propulsion correlate with changes in velocity of the vesicles. The segregation of N-WASP appears mainly driven by Arp2/3-mediated transient interaction of N-WASP with actin filaments. Consistently, vesicles functionalized with the VC fragment of N-WASP which binds

Arp2/3 and branches filaments at a low frequency show a reduced segregation of the nucleator. The presence of the covalent VCA-actin complex at the vesicle surface poisons actin-based movement by preventing detachment of VCA from filaments. These conclusions are supported by a model in which segregation-diffusion of N-WASP is linked to the catalytic cycle of filament transient attachment upon branching. The model quantitatively accounts for the experimentally observed density profiles of N-WASP at the vesicle surface.

MATERIALS AND METHODS

Giant unilamellar vesicles (GUVs) electroformation and functionalization

1,2-Dioleoyl-*sn*-glycero-3-phosphocholine (DOPC) and 1,2-dioleoyl-*sn*-glycero-3-[(*N*-(5-amino-1-carboxypentyl)iminodiacetic acid)succinyl] Nickel salt (DOGS-NTA-Ni) were purchased from Avanti Polar Lipids, Alabaster, AL and stored at -20°C as chloroformous solutions (10 mg/ml for DOPC, 5 mg/ml for DOGS-NTA-Ni). Mixtures of DOPC and DOGS-NTA-Ni in a 9:1 mol/mol ratio were prepared and stored for one month at -20°C .

An original electroformation method was developed, based on the technique described in (27), to obtain 5–10 μm GUVs in the buffer suitable for the experiments, and in a shorter period of time (20 min instead of 3–4 h). To obtain a homogeneous distribution of lipids in liposomes, the miscibility was increased by using phospholipids of identical acyl chains. The phospholipid mixture ($2 \times 10 \mu\text{l}$, at 8.5 mg/ml) was deposited on two indium tin oxide glass plates (10 cm^2) and dried for 2 h under vacuum. The plates were assembled face-to-face and separated by an 800- μm polymer spacer (Gel-Film, from Gel-Pak, Hayward, CA). The chamber was filled with the swelling solution (5 mM Tris-HCl pH 7.8, 1 mM CaCl_2 , 100 μM DTT, 0.01% NaN_3 , and 265 mM sucrose). An alternating electric field of 5 V/mm at 10 Hz was applied between the two plates. The formation of liposomes was directly monitored by phase contrast light microscopy. Once vesicles had reached the desired size (typically 25 μm), the electric field was shut down and the vesicle suspension was carefully extracted to prevent vesicle shearing. The vesicles were stored on ice for 2–3 weeks.

The vesicle concentration was roughly estimated by diluting the original preparation in an isotonic medium (300 mOsm) supplemented with glucose instead of sucrose, allowing sedimentation of the vesicles and facilitating their numbering. According to the estimated concentration, the vesicle suspension was diluted (routinely 5- to 10-fold) in swelling buffer and incubated with 400 nM N-WASP, during at least 3 h.

Proteins

Actin was purified from rabbit muscle (28), isolated in the monomeric (G-actin) form by gel filtration on Superdex-200 and labeled in filamentous form with rhodamine-NHS (cat. No. C1171; Invitrogen, Carlsbad, CA) or Alexa568 Succinimidyl ester (cat. No. A20003; Invitrogen) (29). Recombinant human ADF and gelsolin were expressed and purified as described (30). Profilin was purified from bovine spleen (31). Arp2/3 complex was purified from bovine brain (32) and labeled with Alexa 488 maleimide (cat. No. A10254, Invitrogen) (11). His-tagged human N-WASP was expressed in Sf9 cells using the baculovirus system (32). His-tagged VCA, VC and V constructs derived from N-WASP were bacterially expressed. VCA was obtained by inserting the DNA region of VCA of N-WASP into the pET100/D-TOPO vector. VC and V were obtained by inserting the DNA region in the expression vector pBAD33-GFP (H. Benabdelhak, unpublished data). N-WASP and VC were labeled with Alexa 488 maleimide (11).

The covalent VCA-actin complex was obtained by EDC conjugation (33) as follows. G-actin (15 μM , 40 ml in 5 mM HEPES, 0.2 mM CaCl_2 , 0.2 mM

ATP) was activated with 2 mM EDC and 2 mM sulfo-NHS for 20 min at pH 6.5 at room temperature. One molar equivalent VCA was added (final actin and VCA concentrations were 10 μ M), the pH was adjusted to 7.5 and the reaction was allowed to proceed for 20 min before quenching by 10 mM glycine. The mixture was loaded on 2 ml Ni-Sepharose (GE Healthcare, Waukesha, WI). His-tagged VCA, VCA-actin covalent adduct and a small amount of free actin were eluted with 75 mM imidazole. The eluate was applied to a Superdex G200 16/60 column (Pharmacia, Peapack, NJ) equilibrated in G buffer containing 0.2 mM ADP that weakens the interaction of VCA with G-actin (34), to dissociate most of the noncovalent VCA-actin complex, and 10 μ M Ap5A to inhibit myokinase-mediated ATP production. The gel filtration step was repeated twice in ATP-G-buffer. The covalent VCA-actin complex was recovered 95% pure with 1% final yield (Fig. S4)

Actin polymerization assay

Actin (2.5 μ M, 10% pyrenyl-labeled) was polymerized in F-actin buffer (5 mM Tris-HCl pH 7.8, 1 mM DTT, 0.2 mM ATP, 0.1 mM CaCl₂, 0.1 M KCl, 0.2 mM EGTA and 1 mM MgCl₂) in presence of Arp2/3 complex and nucleator (VC, VCA, or VCA-actin). Polymerization was monitored by the increase in pyrene fluorescence using a spectrofluorimeter (Safas Xenius, Monte Carlo, Monaco).

Motility assay

The vesicle motility medium was adapted from the standard motility medium designed for N-WASP-functionalized polystyrene beads (11) and consisted of 13.5 μ M F-actin, 2.4 μ M profilin, 100 nM gelsolin, 50 nM Arp2/3, 4 μ M ADF in glucose buffer (5 mM Tris pH 7.8, 60 mM KCl, 2 mM MgCl₂, 2 mM ATP, 0.1 mM CaCl₂, 1% (wt/vol) BSA, 0.1% (wt/vol) methylcellulose, 0.01% NaN₃, 1 mM DTT, 0.2 mM DABCO, 50 mM sucrose and 100 mM glucose). Changes in the composition of the medium are indicated in the text. One microliter of functionalized vesicles was added to 9 μ l of motility medium preincubated for 10 min at room temperature to reach the steady state of actin assembly. The solution was placed between a slide and a coverslip, separated by thick hydrophobic walls (~80–100 μ m) drawn using a hydrophobic marker pen (DakoCytomation, Copenhagen, Denmark) to prevent vesicle shearing, and sealed with Vaseline/lanolin/paraffin (Valap, 1:1:1). The samples were observed either in phase contrast or in fluorescence microscopy. Phase contrast imaging was performed using a Diaphot microscope (Nikon, Tokyo, Japan) equipped with a 20 \times air objective (NA 0.5), a motorized stage (Märzhäuser Wetzlar, Pleasanton, CA), and a charge-coupled device camera (Orca II ERG; Hamamatsu, Hamamatsu City, Japan). Fluorescence imaging was performed using an AX70 microscope (Olympus, Melville, NY) equipped with a 60 \times immersion objective (NA 1.42), a motorized stage (Märzhäuser), and an electron-multiplying charge-coupled device camera (Cascade II 512; Photometrics, Tucson, AZ). MetaMorph 6.3 software (Universal Imaging, Burbank, CA) was used for image acquisition, stage control, and the Olympus microscope control. Images were analyzed with MetaMorph and ImageJ (National Institutes of Health, Bethesda, MD) softwares.

Statistical analysis of the types of movement

Static phase contrast pictures were acquired after 1–3 h incubation of the vesicles in the motility medium containing various concentrations of Arp2/3 or gelsolin. Assays were repeated 3–8 times with three different vesicle suspensions, at each given composition of the medium. In each assay, 500–1000 vesicles were randomly selected. Motile behaviors were classified in three categories, identified by the morphology of the actin tails: continuous movement was characterized by a homogeneous actin tail, saltatory movement by periodically dense and light actin tails, and intermediate movement by actin tails showing irregular nonperiodic density changes.

Measurement of the amount of N-WASP bound to the vesicle membrane

The surface density of vesicle-bound N-WASP was evaluated using standard N-WASP-coated beads. Carboxylated polystyrene beads (6 μ m diameter, 2.5% solid, Polysciences, Warrington, PA) were incubated in X buffer (10 mM HEPES, pH 7.8, 0.1 M KCl, 1 mM MgCl₂, 1 mM ATP, 0.1 mM CaCl₂, and 0.01% NaN₃) containing Alexa488-labeled N-WASP at a series of concentrations (0–1.6 μ M) for 1 h at 4°C, under agitation. Further incubation with BSA (10 mg/ml) for 15 min blocked free adsorption sites. Beads were washed twice in 250 μ l X buffer, and suspended at 0.25% solid in X buffer containing 1 mg/ml BSA. The amount of adsorbed protein was determined by SDS-PAGE and immunoblotting using an anti-N-WASP polyclonal antibody and ImageJ analysis (11). Analysis of the supernatants showed that the amount of nonbound activators was negligible. The surface density of immobilized Alexa488-N-WASP (d_s , in molecules per nm²) was derived. Functionalized beads were then observed in fluorescence microscopy. The fluorescence of at least 50 beads was measured in each sample. The fluorescence of Alexa488-N-WASP-coated vesicles was similarly measured and compared to that of Alexa488-N-WASP-coated beads to determine the surface density of N-WASP on the membrane.

Measurement of protein distribution at the vesicle surface

The fluorescence of labeled N-WASP, Arp2/3, and actin was measured along the vesicle contour using MetaMorph 6.3 software. The protein distribution on the surface of moving vesicles was quantified by computing the “segregation ratio”, defined as the ratio of the fluorescence signal integrated over the rear half of the vesicle contour, and the integral over the whole contour. To check that illumination of the vesicles did not interfere with movement and segregation dynamics, static pictures of different vesicles were also taken at different stages of saltatory movement, and the segregation ratio was verified to be compatible with the values of the green curve shown on Fig. 3 B.

In the case of Arp2/3, the fluorescent signal coming from the Arp2/3 incorporated in the actin gel near the surface was subtracted to compute the distribution of Arp2/3 bound to the membrane. This contribution of Arp2/3 in the nearby gel was estimated by measuring the fluorescent signal from actin at the GUV surface, and multiplying it by the local branching density ρ . The branching density at the rear and at the sides of the GUV was considered to be the same as the branching density measured along a cross-section of the actin comet tail. Since the branching density is higher at the center of the comet than at its sides (22), it is higher at the rear of the GUV than at the sides of the GUV. The branching density at the front of the GUV was assumed to be constant and equal to the lowest value of the branching density measured in the actin comet tail. The resulting Arp2/3 profile depends mildly on this assumption: Arp2/3 appears less segregated if we consider a lower branching density at the front of the GUV, but it still remains more segregated than N-WASP, even if the branching density at the front of the GUV is assumed to be 50% lower than the lowest value measured in the comet tail.

The dependence of segregation ratios on a varying parameter, like the concentration of one protein in the motility medium or the density of nucleator at the membrane, was measured on the same batch of vesicles on the same day (from one vesicle batch to another, membrane composition can vary slightly, affecting the activator recruitment, and therefore the motile behavior). For each measurement, segregation ratios were statistically averaged over at least five GUVs in each sample.

RESULTS

Vesicle propulsion occurs in a restricted range of surface density of N-WASP

When placed in the standard motility medium, N-WASP functionalized vesicles first initiated the growth of an isotropic actin

gel at the surface, like N-WASP-coated beads. Propulsion cannot occur unless symmetry of this actin shell is broken by a local rupture in the actin gel that allows the vesicle to escape. The mechanism of symmetry-breaking that precedes the establishment of polarized movement differs for fluid vesicles and solid beads, as analyzed in detail elsewhere (22). Briefly, the location of the break is defined by a local lower actin density at the vesicle surface, while for beads it starts with the fracture of the outer region of the gel. The pressure developed by the growth of the actin gel around the actin-bound lipid surface enhances the local weakness of the gel, induces the formation of an expanding zone of low filament density, and eventually pushes the vesicle out of this zone. This process develops in 30 min, while the break of symmetry of the actin gel leading to polarized movement of solid beads occurs within a few minutes. The formation of a zone of low actin density at the vesicle surface implies that local inhomogeneities in N-WASP density can occur, which is possible only in a restricted range of global N-WASP densities.

The surface density of N-WASP was controlled either by the density of Ni-NTA-derivatized lipids that bind His-tagged N-WASP, or by the concentration of N-WASP during the functionalization step. An optimum surface density of 0.19 ± 0.06 molecules/100 nm², corresponding to a mean distance of 23 nm between nearest neighbors, was required for vesicles to break symmetry and be propelled. These conditions were met by incubating vesicles containing 10% Ni-lipids in the presence of 400 nM N-WASP for 3 h. At lower densities of N-WASP, the actin meshwork lacked the cohesive structure required for a break to occur, and the

vesicle remained nonmotile, entrapped in a homogeneous actin shell. At high densities of N-WASP, the pressure developed by the growth of a dense actin gel was high enough to cause the collapse of the vesicles before symmetry was broken (Fig. S1 A). In some cases, fission events were recorded, in which a fraction of the vesicle budded out and was expelled while the force developed by actin assembly was sufficient to cause the contraction of the lipid “neck”, thus entrapping the remaining fraction of the vesicle in the actin gel. The former, expelled vesicle generally propelled itself with an actin tail, while the latter vesicle remained surrounded by a dense actin gel and was nonmotile.

The process is reminiscent of the macropinocytosis events reported and analyzed *in vivo* (35,36). Similar fission events are generated when N-WASP present in cell extracts is recruited at the surface of ARF1-coated GUVs (23).

The motile behavior of N-WASP-functionalized GUVs is controlled by Arp2/3 complex

Once expelled from the actin gel, N-WASP functionalized vesicles displayed a variety of motile behaviors, from a continuous regime of propulsion with a homogeneous actin tail (Fig. 1 A), to a periodic “saltatory” regime that was characterized, in phase contrast microscopy, by alternating light and dark (i.e., dense) regions, in steps of a few microns (Fig. 1 B and Movie S2 in Data S1). Based on fluorescence measurements, the actin concentration was 1.5–2.5 times higher in the dark than in the light regions. Small (<5 μm in

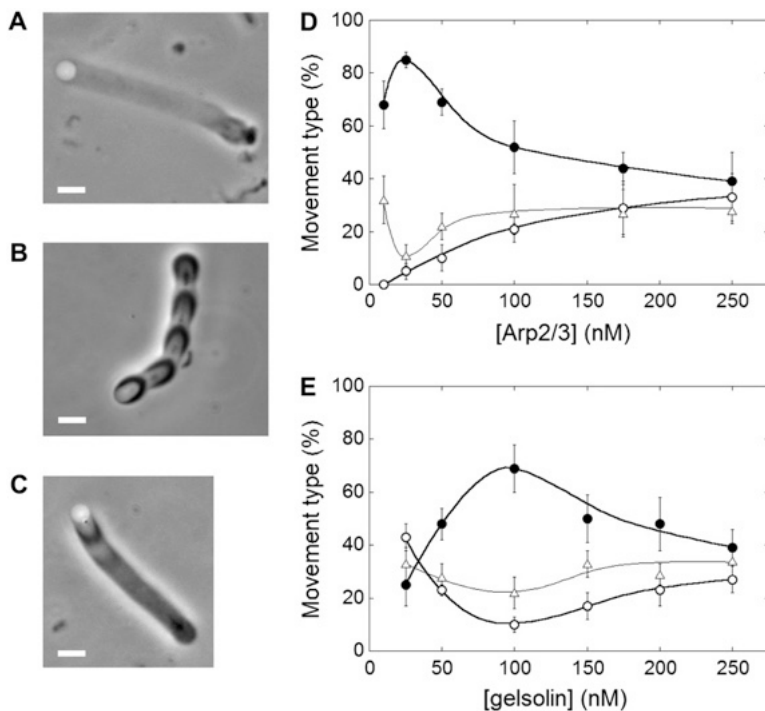


FIGURE 1 The biochemical composition of the medium affects the motile behavior of GUVs. Phase contrast images of N-WASP-functionalized vesicles placed in a motility medium (50 nM Arp2/3 and 100 nM gelsolin), and undergoing saltatory (A), continuous (B), and intermediate (C) movement. Scale bars = 10 μm. Graphs show the percentage of vesicles undergoing saltatory (solid circles), continuous (open circles), and intermediate (triangles) movement as a function of Arp2/3 concentration, at 100 nM gelsolin (D); and as a function of gelsolin concentration, at 50 nM Arp2/3 (E). The curves are a guide to the eye. Each data point corresponds to an average over a collection of 3–8 vesicle preparations. Error bars indicate the standard deviation.

diameter) as well as large ($>10\ \mu\text{m}$ in diameter) vesicles exhibited both types of movement. Only vesicles undergoing a regular periodic movement, with a defined step size, were classified as “saltatory”. Chaotic behaviors in which the saltatory movement was not regularly periodic were also recorded and defined as “intermediate” movement (Fig. 1 C).

In the continuous regime, vesicles move at constant velocity, while in the saltatory regime vesicles repeat the initial expulsion process in a cycling fashion (see Movie S2, in Data S1, and (22)). The directionality of propulsion is determined by the primary expulsion step, which defines the front and rear regions, and is maintained all along the trajectory. The velocity of the saltatory vesicles varied periodically, with maximal speed (peak velocity can reach over $10\ \mu\text{m}/\text{min}$) correlating with regions of lower actin density. Similar saltatory behaviors have been observed with solid particles (8,22,37), oil droplets (26), or mutated *Listeria* (38,39). The saltatory propulsion of liposomes offers a unique opportunity to understand the mechanistic links between the force produced by actin polymerization, the deformation of the membrane, the diffusion of N-WASP in the lipid bilayer, and the velocity of the GUV.

To determine whether changes in the frequency of filament branching were responsible for the saltatory movement, we measured the Arp2/3:actin ratio, which represents the branching density of the actin meshwork, using double fluorescence measurements of Alexa488-Arp2/3 and rhodamine-actin (11) (Fig. S2). The branching density was constant along the axis of the actin tail of continuously propelled vesicles, as reported in the case of beads (11). The branching density was also mostly constant, or increased slightly up to 30% in dense actin regions, along the tails of saltatory vesicles. The poor correlation of these modest changes in filament branching density with the periodicity observed in phase contrast suggests that saltatory motion is not due to periodic changes in the rate of filament branching.

The dependence of the motility regime on the concentrations of Arp2/3 (which controls the rate of filament branching) and gelsolin (which controls the rate of filament capping) was examined (Fig. 1, D and E). A statistical analysis showed that the saltatory motion was predominant at low Arp2/3 concentration: nearly all vesicles exhibited a hopping behavior at 25–50 nM Arp2/3, but only 40% did so at 250 nM Arp2/3. Almost no movement was detected at Arp2/3 concentrations $<25\ \text{nM}$. A bell-shaped gelsolin concentration dependence of saltatory movement was observed, with a maximum at 100 nM gelsolin, similarly to the gelsolin-dependence of the velocity of beads in a continuous regime of motion (11).

These results suggest that a threshold rate of filament branching by the membrane-bound N-WASP-Arp2/3 complex is required for GUVs to perpetuate the formation of the actin tail and move at constant velocity. The following experiments were performed to understand how the transition from continuous to saltatory movement is controlled.

Saltatory and continuous movement: the role of N-WASP distribution

To understand which molecular reactions occur at the liposome-filament interface and determine saltatory propulsion, we measured the time course of deformation and velocity of the vesicle by tracking the front and the rear boundaries during one step. Time $t = 0$ is defined as the beginning of a cycle, when the vesicle is at rest. The sequence of events corresponding to a saltatory cycle decomposed in three phases, referred to as phases I, II, and III as follows (Fig. 2):

Phase I ($t = 0$ to $t = 350\ \text{s}$, for the GUV shown in Fig. 2).

The vesicle initiates a (quasi)symmetrical actin shell, which breaks open typically at $t = 40\ \text{s}$ (Fig. 2). The vesicle gradually elongates as it is pushed out of the actin shell, over a time period from $t = 40\ \text{s}$ to $t = 350\ \text{s}$. In this process, the center of mass moves at $\sim 0.5\ \mu\text{m}/\text{min}$ (average between front and rear velocities).

Phase II ($t = 350\ \text{s}$ to $t = 470\ \text{s}$) covers the rapid expulsion and relaxation of the deformation of the GUV. The rear of the vesicle rapidly detaches from the actin gel, the vesicle moves out of the actin shell, a velocity peak of at least $10\ \mu\text{m}/\text{min}$ is reached, while the vesicle recovers a quasi-spherical shape.

Phase III ($t = 470\ \text{s}$ to $t = 680\ \text{s}$). After expulsion, the vesicle gradually slows down until it stops.

During phase I, movement is slow and mainly results from the deformation of the vesicle due to the compression by the growing actin shell. During phase II, rapid movement results from the mechanical conversion of the energy stored in vesicle deformation. During phase III, the shape of the GUV remains unchanged, and movement is driven by the polymerization of actin that slows down gradually until the vesicle stops.

The new actin shell formed at the end of phase III, at the onset of a new cycle, is not perfectly symmetrical. The preferential formation of the actin gel at the rear of the vesicle biases the direction of the next step.

Phases I and II represent the break of symmetry and the escape of the GUV out of the dense actin shell, which initiate both saltatory and continuous propulsive movements. However, in continuous movement the vesicle does not slow down during phase III. To get insight into the molecular mechanism that controls the switch from continuous to saltatory movement in phase III, we sought distinctive physical and chemical parameters of the vesicles in the two regimes, as follows.

The extent of deformation of the vesicles did not correlate with a particular motile behavior. In continuous movement as well as in phase III of saltatory movement, large differences in the extent of deformation among vesicles were recorded. Some vesicles remained spherical in either regime. This is probably due to variations of the elastic properties between

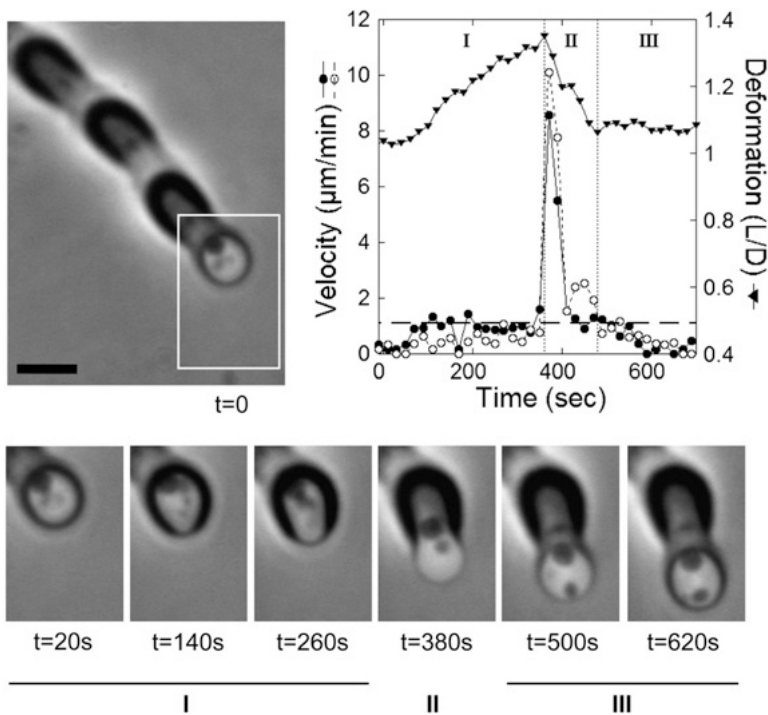


FIGURE 2 Kinetic analysis of the deformation and velocity of a GUV during saltatory propulsion. A $8.1\text{-}\mu\text{m}$ diameter vesicle propels in steps of $13\text{ }\mu\text{m}$, every 680 s (average velocity is $1.14\text{ }\mu\text{m}/\text{min}$), in standard motility medium (top left). A time-lapse phase contrast image of one of the steps is shown in bottom panel. Scale bar = $10\text{ }\mu\text{m}$. The graphs (top right) show the velocities of the front (solid circles, solid line) and the rear (open circles, dashed line) of the vesicle, and vesicle deformation, i.e., its length L divided by its average diameter D (triangles), as a function of time. The horizontal dashed line indicates the average velocity of vesicles moving continuously, under the same conditions: $1.1 \pm 0.3\text{ }\mu\text{m}/\text{min}$. The vertical dotted lines mark the boundaries of the three different phases that make one step: deformation (I), expulsion (II), and slowing down (III). Data points are 20 s apart. Time $t = 0$ corresponds to the beginning of a period, when the vesicle is stopped. The data points represent measurements averaged over four subsequent steps.

different vesicles, allowing more or less deformation during the expulsion step.

In previous studies of actin-based propulsion of fluid objects, a higher density of nucleators at the rear of the object during movement was observed (21,24–26). We therefore analyzed the distribution of fluorescently-labeled N-WASP on vesicles during continuous or saltatory movement comparatively, by computing the segregation ratio, which represents the fraction of the observed N-WASP population that is located in the rear half of the contour of the vesicle (Fig. 3 A). Note that all measurements were carried out with the same average surface density of N-WASP). During saltatory propulsion, the value of this ratio cycles between 0.5, corresponding to a homogeneous distribution of the N-WASP population, effectively measured at time zero, and 0.6, corresponding to a 1.5-fold higher surface density of N-WASP in the rear than in the front half of the vesicle (Fig. 3 B). The segregation ratio increases up to 0.6 during phases I and II, as the vesicle is expelled from the actin shell, and decreases steeply to 0.5 during phase III, as the vesicle slows down and stops. Hence phase III corresponds to the evolution of N-WASP distribution from a segregated to a uniform distribution.

During continuous movement, the high value of the segregation ratio (0.60 ± 0.03 in standard GUV motility conditions) reached upon expulsion from the initial actin shell was subsequently maintained (green dashed line in Fig. 3 B). These results are in agreement with independent data from Giardini et al. (21), showing an asymmetric distribution of ActA (another activator of Arp2/3) at the surface of contin-

uously moving vesicles. We derived a rough estimate of 0.64 for the ActA segregation ratio in Giardini et al.'s data. In another study, a very strong segregation of VCA (the constitutively active part of N-WASP), corresponding to the gathering of 90% of the VCA molecules at the rear of continuously moving oil droplets, was reported (25).

In a recent study by Trichet et al. (26), it was proposed that the saltatory movement of VCA-coated oil droplets placed in cell extracts supplemented with VASP could result from variations in the distribution of VCA at the droplet surface, but no measurements were presented. Here we show evidence for a direct correlation between the maintenance of nucleator segregation and continuous movement. We further show that in saltatory movement, the changes in velocity correlate with changes in nucleator distribution. Constant velocity correlates with a highly segregated distribution of N-WASP. The decrease in velocity (phase III) correlates with the loss of N-WASP segregation (Fig. 3 B). A segregation ratio of 0.60 ± 0.03 was averaged over vesicles undergoing continuous propulsion, with a minimum value of 0.55. For vesicles in saltatory movement, we observed that the segregation ratio typically dropped below 0.55 during phase III. Thus, a threshold value of ~ 0.55 marks the transition from the saltatory to the continuous regime of propulsion.

To elucidate whether the segregation of N-WASP is at the origin or arises as a consequence of a particular type of motile behavior, the chemical reactions that establish the link between N-WASP and the actin meshwork must be analyzed in detail. An important issue concerns the permanent or transitory nature of these links during movement. This point is

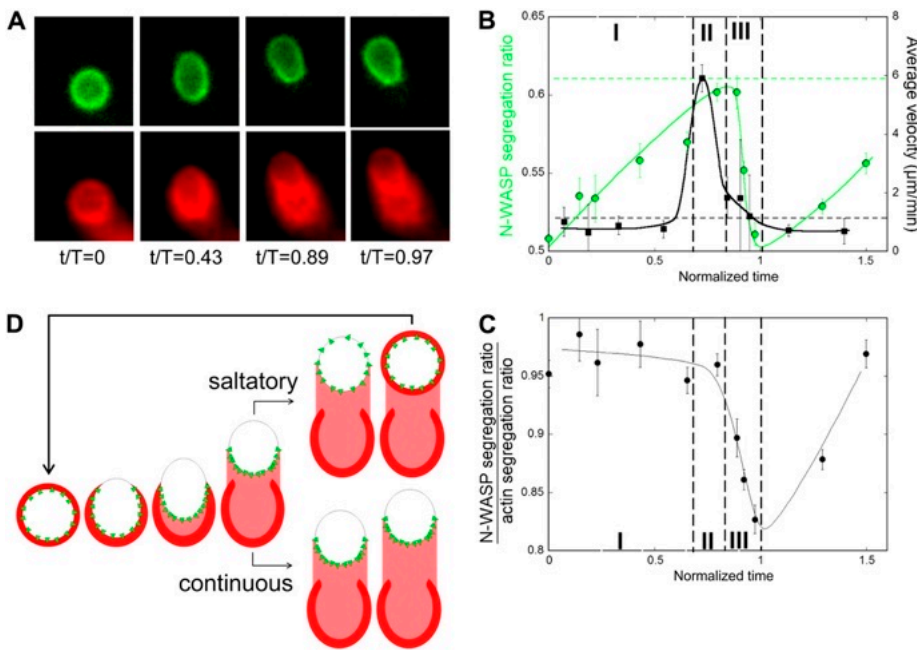


FIGURE 3 Segregation of N-WASP and actin during a saltatory step. (A) Double-fluorescence of Alexa 488-labeled N-WASP (in green) and rhodamine-labeled actin (in red) of a vesicle (3.3 μm diameter) during a saltatory step. Normalized time (i.e., time t divided by saltatory period, T) is indicated. (B) Change in the N-WASP segregation ratio (green circles), and in the average velocity of the vesicle (black squares) during one step. Each data point corresponds to the mean of six measurements carried out on the same picture, and error bars indicate the standard error of these measurements. The solid lines are guides to the eye. The green dashed line represents the N-WASP segregation ratio for continuous movement, obtained by a single measurement on a GUV of similar size (3.5 μm diameter) in the same sample. It is consistent with the average value measured for continuous movement over different samples, in the same conditions. The black dashed line represents the average velocity of seven vesicles moving continuously in the same conditions.

tions. (C) Relative variations of N-WASP and actin segregation ratios during the same saltatory cycle. The solid line is a guide to the eye. The timescale is normalized as in panel B. The vertical dashed lines indicate the three phases of saltatory movement (see text and Fig. 2). (D) Schematic representation of N-WASP distribution (green triangles) on the vesicle, during its escape from the actin shell (in red) and subsequent movement: if the interaction of N-WASP with filament is sufficient to maintain segregation, continuous movement is sustained; if diffusion of N-WASP dominates, segregation is lost and movement stops, resulting in saltatory behavior.

addressed by image analysis of the correlated distributions of N-WASP and actin at the surface of the vesicles during movement. Another type of independent information can be obtained either by replacing the original N-WASP nucleator by N-WASP derivatives chemically modified to display an altered filament branching activity, or by interfering with N-WASP function by addition of dead-end adducts. The following experiments were designed.

N-WASP molecules bind transiently to actin filaments

In continuous movement, the distributions of actin and N-WASP at the surface of vesicles are qualitatively similar, actin being more segregated than N-WASP (0.72 ± 0.07 and 0.60 ± 0.03 , respectively). The distributions of actin and N-WASP were analyzed comparatively during a saltatory cycle, during which N-WASP cycles between a segregated and a homogeneous distribution (Fig. 3 B). We observed that the actin segregation ratio cycles similarly, except for a delayed loss of actin segregation compared to that of N-WASP during phase III. This behavior is evidenced by monitoring the evolution of the N-WASP segregation ratio divided by the actin segregation ratio (Fig. 3 C):

In phases I and II, N-WASP and actin co-segregate, and the actin meshwork and N-WASP make a cohesive

vesicle-bound structure that causes deformation and expulsion of the vesicle. The fast release of the rear of the vesicle from the gel is followed by a slower process (~ 100 s, phase II) allowing the vesicle to escape from the shell and resume a (nearly) spherical shape. In other words, during phases I and II, the actin gel holds the vesicle back, and the links between N-WASP and the actin filaments prevent its free diffusion in the lipid bilayer and cause its segregation. As filaments sweep N-WASP molecules toward the rear of the vesicle, N-WASP segregation reaches a maximum after the vesicle's escape from the actin shell.

During phase III, N-WASP returns to a homogeneous distribution before actin (drop in the curve in Fig. 3 C), indicating that some N-WASP molecules, formerly bound to filaments, become free to diffuse in the lipid bilayer. If the whole population of N-WASP was in a freely-diffusing state, N-WASP would spread homogeneously over the whole vesicle within a few seconds. The fact that it takes several tens of seconds for N-WASP to return to a nonsegregated state implies that exchanges take place between populations of bound and free N-WASP molecules.

In conclusion, the bonds between N-WASP and the filaments are transient, and drive the segregation of N-WASP at the rear of the GUV, while free diffusion tends to distribute

N-WASP homogeneously around the GUV. Fig. 3 *D* summarizes the consequence of these molecular interactions on the GUV motile behavior: it schematically shows the escape of a vesicle from its initial actin shell and the resulting segregation of N-WASP, along with the two possible subsequent motions, depending on whether N-WASP segregation is lost or maintained.

The Arp2/3 complex drives N-WASP segregation at the rear of the vesicles

The fact that continuous movement is favored by high Arp2/3 concentrations (Fig. 1) suggests that Arp2/3 plays an important role in strengthening the link between N-WASP and the filaments to maintain segregation (Fig. 3 *D*). This hypothesis was challenged by analyzing the dependence of N-WASP segregation on Arp2/3 concentration, and by monitoring the segregation of Arp2/3 during movement.

The N-WASP segregation ratio was measured at different Arp2/3 complex concentrations on continuously moving GUVs of $4 \pm 0.5 \mu\text{m}$ -radius, from the same GUV preparation (from one vesicle batch to another, N-WASP recruitment, and therefore the motile behavior, can vary). Segregation ratios of 0.60 ± 0.03 and 0.69 ± 0.02 were measured at 100 nM and 250 nM of Arp2/3 complex, respectively. These data indicate that the binding of Arp2/3 to N-WASP significantly enhances the attachment of filaments to N-WASP during movement.

If Arp2/3 complex is responsible for N-WASP segregation by mediating the link with the filaments, it should segregate as well at the rear of the GUVs in continuous propulsion. We thus measured the Arp2/3 segregation ratio (see Materials and Methods, and Fig. S3) and compared it to that of N-WASP. The segregation ratio of Arp2/3 was 0.75 ± 0.07 , while the segregation ratio of N-WASP was only 0.60 ± 0.03 in the same conditions. Considering that the Arp2/3 complex present at the surface is necessarily bound to N-WASP, it hereby corresponds to a subpopulation of N-WASP: Arp2/3-bound N-WASP. Therefore, this subpopulation of N-WASP is more segregated than the total N-WASP population. This implies that the Arp2/3 complex drives the segregation of N-WASP. In other words, N-WASP exists in a minimum of three states: a free state, an Arp2/3-bound state, and a state in which it is bound to both Arp2/3 and an actin filament. In the first two states, N-WASP and N-WASP-Arp2/3 can diffuse freely, while in the last state, N-WASP and Arp2/3 are bound to actin, and are segregated at the rear of the GUV.

To further investigate the role of the Arp2/3 complex in the binding of N-WASP to filaments and its segregation at the rear of GUVs, we functionalized GUVs with fragments of N-WASP that interact more or less strongly with the Arp2/3 complex.

In cells, N-WASP is folded in an almost inactive conformation. When activated by signaling molecules, it exposes its catalytic C-terminal domain, called VCA. The VCA domain of N-WASP constitutively branches filaments with Arp2/3

complex in solution. In motility assays, it has been shown that N-WASP is fully activated when adsorbed at the surface of polystyrene beads (11) or bound to Ni-derivatized lipids on vesicles (22) and behaves as VCA.

We first recorded the polymerization properties of different constructs: VCA, VC, and V (Fig. 4 *A*), which have different affinities for Arp2/3 complex but bind G-actin with identical affinity and in a functionally identical fashion (J.-F. Gaucher, unpublished data). In pyrenyl-actin fluorescence polymerization assays, V failed to induce autocatalytic branching of actin filaments, even in the presence of Arp2/3 complex (data not shown), while VC required ~ 50 -fold higher amounts of Arp2/3 than VCA to branch filaments (Fig. 4 *B*).

The motile behavior of GUVs functionalized with full-length VCA or its truncated fragments VC and V was then recorded in the standard medium containing 100 nM Arp2/3 complex. The VCA-coated vesicles behaved identically to N-WASP-coated vesicles. V-coated vesicles did not initiate actin assembly and did not move, as expected from polymerization assays, since V does not bind Arp2/3. VC-coated

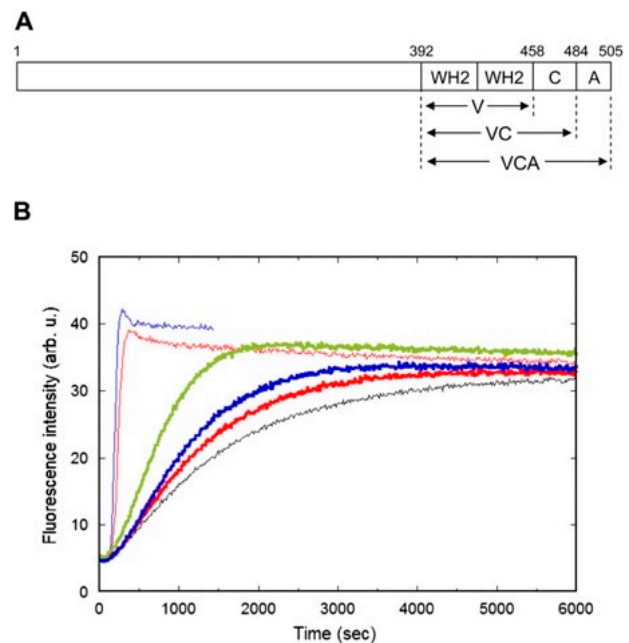


FIGURE 4 The VC fragment of VCA fails to stimulate actin polymerization in branched filaments. (A) Domain structure of N-WASP and derived fragments. All constructs are histidine-tagged to allow recruitment on GUVs. Abbreviations for the different fragments are used in the text as follows: VCA (residues 392–505) contains the two WH2-domains that bind G-actin and the CA-domain that binds the Arp2/3 complex; VC (residues 392–484) is VCA deleted from the acidic domain that stabilizes the interaction with Arp2/3; and V (residues 392–458) is WH2-domains. (B) Pyrenyl-actin polymerization assay: 2.5 μM actin were polymerized alone or in the presence of 34 nM Arp2/3 (thin black curve—the two curves superimposed, and only one is shown); in presence of 17 nM Arp2/3 with 312 nM VC (thick red curve) or 312 nM VCA (thin red curve); in presence of 34 nM Arp2/3 with 312 nM VC (thick blue curve) or 312 nM VCA (thin blue curve); and in presence of 84 nM Arp2/3 with 312 nM VC (thick green curve).

GUVs, in contrast with the weak activation of Arp2/3 by VC in polymerization assays, generated actin gels that broke symmetry and led to the propulsion of the vesicles, at a rate at least equal to the rate of N-WASP- or VCA-coated vesicles. Note that, in a motility assay, there is a strong heterogeneity between the vicinity of the GUV's surface, where proteins are concentrated and branching reactions are frequent, and the bulk of the medium, where nucleators are nearly absent. This heterogeneity allows the nucleator to be locally concentrated, without lowering the amount of G-actin available in bulk, as it would (by sequestering) if it were concentrated everywhere (32). This effect enhances the activity of VC in motility assays compared to polymerization assays in solution. At lower concentrations (50 nM) of Arp2/3 complex, VC-coated GUVs were unable to move. The following measurements were all carried out at 100 nM Arp2/3, on GUVs undergoing continuous movement.

The VC segregation ratio measured using Alexa488-labeled VC, was 0.52 ± 0.02 , while actin around the same GUVs had a segregation ratio of 0.65 ± 0.02 . This result clearly demonstrates that VC segregates much less than N-WASP during continuous motion of GUVs. The weak segregation of VC indicates that VC interacts more weakly with actin filaments than N-WASP. VC- and VCA-functionalized vesicles were monitored together in the same motility assay containing rhodamine-actin and Alexa488-Arp2/3. The branching density derived from the double fluorescence measurements was roughly twofold lower in comet tails of VC-GUVs than VCA-GUVs.

Since the segregation of the nucleator and of actin are interdependent, we compared the segregation of N-WASP and VC when they are both interacting with the same actin filament network. To do so, we functionalized GUVs with both N-WASP and VC, one of which being fluorescently labeled. The fluorescence of the labeled nucleator at the GUV surface decreased upon increasing the fraction of the unlabeled nucleator, indicating that both were recruited with equal efficiency via their His-tag. The segregation of N-WASP, VC, and actin was evaluated as a function of the percentage of N-WASP and VC (Fig. 5 B). N-WASP was more segregated than VC, on all GUVs, showing that the nucleator's affinity for Arp2/3 affects its interaction with actin filaments, and modulates its segregation.

The segregation ratio of VC was unaffected by the presence of N-WASP, and remained at the value of 0.52 ± 0.01 , from 0 to 75% N-WASP (Fig. 5 B). Below 50% VC, the presence of VC did not affect the segregation ratios of actin and N-WASP, which remained identical to the values measured on 100% N-WASP-coated GUVs (0.72 ± 0.07 for actin, and 0.60 ± 0.03 for N-WASP). At 75% VC, the segregation ratio of N-WASP was slightly lower (0.56 ± 0.03). Above 50% VC, the segregation ratio of actin decreased to 0.65 ± 0.02 (for 100% VC-coated vesicles) as the percentage of VC increased (as a reference, the segregation ratio of actin is 0.59 ± 0.02 for solid beads presenting a homogeneous

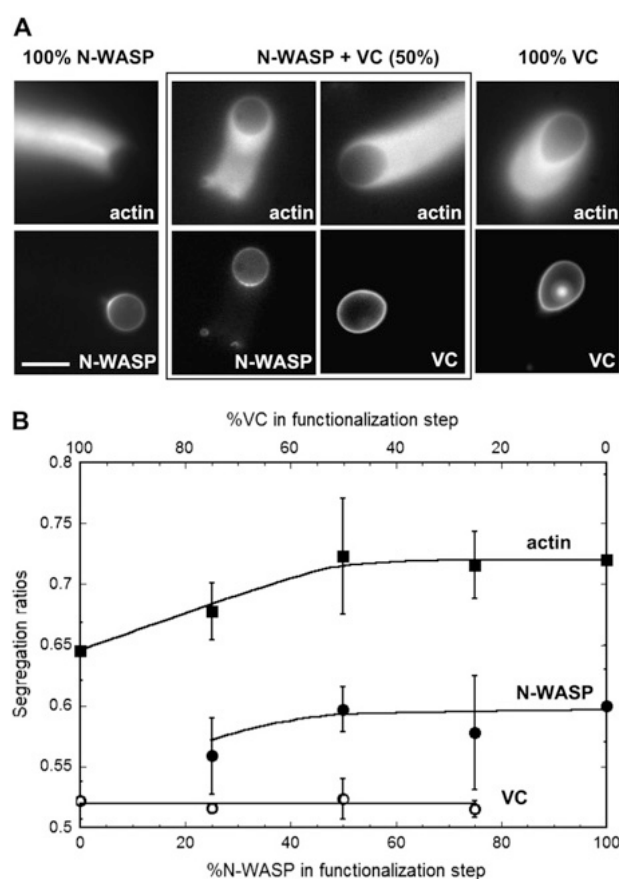


FIGURE 5 The VC fragment of N-WASP is sufficient to induce vesicle propulsion, with a lower extent of segregation. (A) Fluorescent images of GUVs coated with a mixture of N-WASP and VC: 100%, 50%, and 0% of N-WASP, from left to right. (Top) Alexa568-labeled actin comets; (bottom) Alexa488-labeled N-WASP or VC on the GUV surface. Scale bar = 10 μ m. (B) Segregation ratios of labeled actin (squares), N-WASP (solid circles), and VC (open circles) at the surface of GUVs undergoing continuous propulsion, as a function of the N-WASP content used during GUV functionalization. Error bars indicate standard deviations. Lines are guides to the eyes.

distribution of nucleators (22)). These data indicate that, in presence of both N-WASP and VC, the segregation of actin is mainly dictated by its interaction with N-WASP, which binds more strongly to Arp2/3.

The release of actin from VCA is required for movement

The catalytic VCA domain of N-WASP binds not only Arp2/3 but also a G-actin molecule with the V (WH2) domain. The binding of G-actin to the V moiety of VCA is known to be essential for filament branching (13). The isolated V domain by itself, presented on the surface of a lipid-coated bead, binds G-actin and mediates the transient attachment of the WH2-actin complex to a filament barbed end, a reaction con-

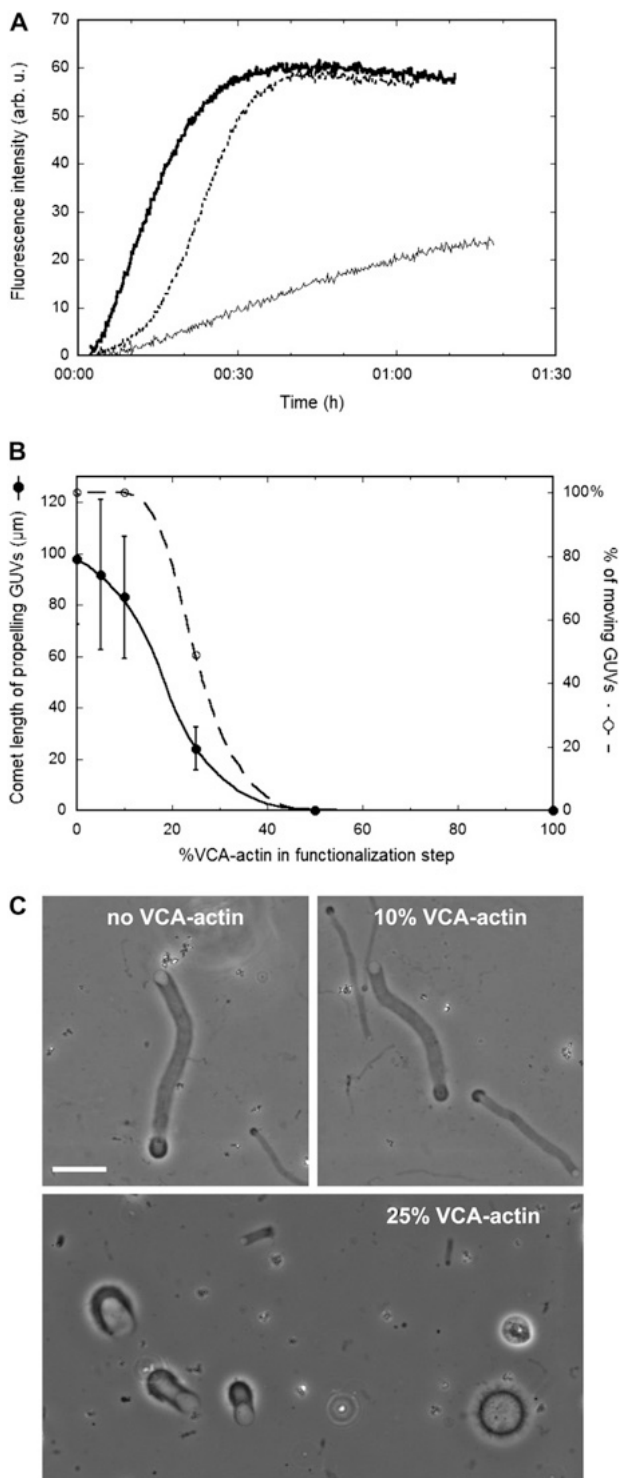


FIGURE 6 VCA-actin covalent complex stimulates polymerization in branched filaments with Arp2/3 complex in solution, but inhibits vesicle movement when anchored at the surface of GUVs. (A) Pyrenyl-actin polymerization assay: 2.5 μM actin were polymerized alone (*thin solid curve*), in presence of 30 nM Arp2/3 supplemented with 125 nM of either VCA (*dashed curve*) or VCA-actin (*thick solid curve*). (B) Percentage of propelled VCA-functionalized GUVs (*open circles*) and average comet

length (*solid circles*), after 1 h incubation in the motility medium, as function of the fraction of VCA-actin used during functionalization. The lines are guides to the eyes. (C) Images of vesicles after 1 h incubation in the motility medium, functionalized with a mixture of VCA and 0%, 10%, and 25% VCA-actin, from left to right, respectively. Scale bar = 20 μm .

sistent with known properties of WH2 domains (32,40–42). Although the structural details of the formation of the branched junction by association of the ternary VCA-actin-Arp2/3 complex with a filament are not known, the available data from different groups altogether support the view that VCA branches a filament by making two contacts with a filament, via V-actin and the CA-Arp2/3 subcomplexes. While our data show the importance of the CA-Arp2/3 attachment to a filament, whether the V-actin-filament attachment plays a role in the process is not clear. To address this issue, we covalently coupled VCA to a G-actin molecule by the zero-length cross-linker EDC and isolated the covalent VCA-actin adduct. In solution, VCA-actin covalent complex branched the filaments as efficiently as VCA (Fig. 6 A). However, in contrast with VCA (*dashed curve*), polymerization in presence of VCA-actin (*thick solid curve*) starts immediately without a nucleation lag as the covalent complex acts as a nucleus that initiates filament polymerization.

GUVs functionalized with VCA-actin covalent complex appeared unable to initiate an actin gel and move, even after hours of incubation in the motility medium, at any concentration of Arp2/3. When fluorescently-labeled actin was present in the motility medium, no fluorescence was detected around the VCA-actin functionalized vesicles. This result contrasts with the ability of VCA-actin covalent complex to polymerize actin in branched filaments in solution. Therefore the VCA-actin complex is able to form a branch junction but seems unable to detach from it. This behavior has no impact on polymerization assays, where the number of branch junctions that are formed is much lower than the number of nucleators available in solution (30), but it does not allow motility, where nucleators must be able to detach from the filament and form new branches, over and over. The surface of a GUV functionalized with the VCA-actin complex would hence be covered with independent, anchored actin filaments, which cannot grow into a detectable network and lead to propulsion.

Vesicles were then functionalized with mixtures of VCA and VCA-actin covalent complex. The percentage of comet-propelled vesicles, as well as the average length of the formed comet tails, were measured after 1 h, as a function of the proportion of VCA-actin in the functionalization mixture (Fig. 6 B). As little as 10% VCA-actin complex decreased the length of the actin tails formed after 1 h. With 25% VCA-actin, 50% of the GUVs grew actin gels but failed to generate movement, and the average length of the propelled GUVs was decreased fourfold. At 50% VCA-actin, the GUVs were surrounded by actin gels and no comet tails were formed. Identical results were obtained either keeping the total amount of VCA and VCA-actin constant (500 nM) in the

length (*solid circles*), after 1 h incubation in the motility medium, as function of the fraction of VCA-actin used during functionalization. The lines are guides to the eyes. (C) Images of vesicles after 1 h incubation in the motility medium, functionalized with a mixture of VCA and 0%, 10%, and 25% VCA-actin, from left to right, respectively. Scale bar = 20 μm .

functionalization step, or keeping the amount of VCA constant (500 nM) and adding increasing amounts of VCA-actin.

These data indicate that the VCA-actin complex may “poison” the nucleating function of VCA at the vesicle surface: not only does its presence lower the actual surface density of VCA, but it also strongly anchors actin filaments. If these anchored filaments are connected to the rest of the actin network, they could prevent its growth by holding it against the surface.

In conclusion, dissociation of VCA from both actin and Arp2/3 complex is required for detachment of filaments from VCA and for actin-based motility.

DISCUSSION AND MODEL

The analysis of reconstituted actin-based propulsion of N-WASP functionalized GUVs has provided insight into physiologically relevant aspects of motile processes that take place at the interface between actin filaments and membranes like at the tip of lamellipodia or in endosome propulsion, macropinocytosis, or phagocytosis. Recent *in vivo* studies have pointed out to mutual interactions between the barbed ends of actin filaments and membrane components at the leading edge (20). This simple system in which N-WASP is bound to a lipid bilayer with no intermediates demonstrates that the force produced by the actin machinery against the membrane is by itself sufficient to reconstitute membrane deformation and fission (23) like *in vivo* (35,36).

Membrane fluidity and deformability play active roles in actin-based propulsion of GUVs. The physical characteristics of the saltatory regime of propulsion of GUVs differ from those of actin-propelled solid microbeads (22,37), as well as from the nanosaltation of *Listeria* (43,44). Trichet et al. (26) have recently observed a very similar hopping behavior, with VCA-coated oil droplets placed in cell extracts supplemented with VASP. Although variations in VCA distribution on the droplets during hopping movement have not been detected, the authors propose that the saltatory movement operates by a segregation-diffusion mechanism, in which VASP enhances filament detachment from VCA. Perhaps detachment is enhanced to such an extent that VCA molecules are abruptly released from filaments and very rapidly diffuse to a homogeneous distribution around the droplet. The maintenance of a strong actin segregation (which was not measured, but can be inferred from microscopy images—Fig. 6 of (26)—and from the observation that the droplets do not come to a complete stop) could allow VCA to rapidly return to a segregated distribution, and would explain why variations in VCA distribution could not be observed. Considering the actin distribution as a parameter that drives nucleator segregation is one of the points on which our description of the mechanism differs from that of Trichet et al. (26), as we explain in the next section (model).

Remarkably, observations made at the mesoscopic scale provide a mechanistic and kinetic insight into molecular

processes that orchestrate cell motility, which cannot be derived from solution studies of polymerization of actin in branched filaments. Each membrane-immobilized nucleator uses Arp2/3 complex and G-actin in multiple catalytic cycles of filament branching coupled to its attachment-detachment from the filament barbed ends. The data demonstrate that the segregation of N-WASP is due to the transient attachment of filaments to membrane-bound N-WASP-Arp2/3. This result does not support the actoclampin model (18,19). On the contrary, our results support the tethered ratchet model, where filaments alternate between elongation and binding (17). The fact that the covalent attachment of the WH2 domain of VCA to actin blocks movement, is consistent with the conclusions of Co et al. (16) that the WH2 domain by itself captures barbed ends independently of the Arp2/3 complex. However, the fact that VC, which interacts weakly with Arp2/3, segregates very weakly on GUVs, demonstrates that the interaction of WH2 domains with filament barbed ends is in itself insufficient to drive segregation of VC. Hence, the association of the Arp2/3 complex to the CA domain of N-WASP plays a dominant role in mediating the attachment of barbed ends to N-WASP.

Our kinetic analysis of saltatory propulsion, shows that, except for the local detachment at the rear (onset of phase II), the vesicle remains in contact with the actin gel throughout its movement. If contact was lost by some slippage event, the vesicle would stop immediately after its escape from the actin shell, and N-WASP molecules would quickly diffuse and recover a homogeneous distribution over the whole membrane. On the contrary, the decline in velocity associated with the gradual return of N-WASP to a homogeneous distribution corresponds to the dissociation of N-WASP from Arp2/3 after incorporation of Arp2/3 in a branched junction. These data provide the first demonstration that once N-WASP dissociates from filament-bound Arp2/3, it is no longer tethered to the filament. After detachment from the branched junction, N-WASP is in a state in which it freely diffuses in the lipid bilayer. At high enough Arp2/3 concentration, the rapid binding of a new Arp2/3 complex molecule to N-WASP occurs, thus allowing rapid reassociation with a filament and maintenance of sustained movement.

It is likely that in the reconstituted motility assay, the concentration of G-actin is maintained at a high enough value to saturate the WH2 domain. We propose that N-WASP therefore exists mainly in three states: a free state and an Arp2/3-bound state, in both of which it diffuses freely at the surface of the GUV, and a filament-attached state in which its diffusion is hampered (Fig. 7).

Model of the segregation-diffusion mechanism of N-WASP

The ability of the proposed mechanism of segregation and diffusion orchestrated by the cycle of filament branching (Fig. 7) to generate the main features of the density profiles

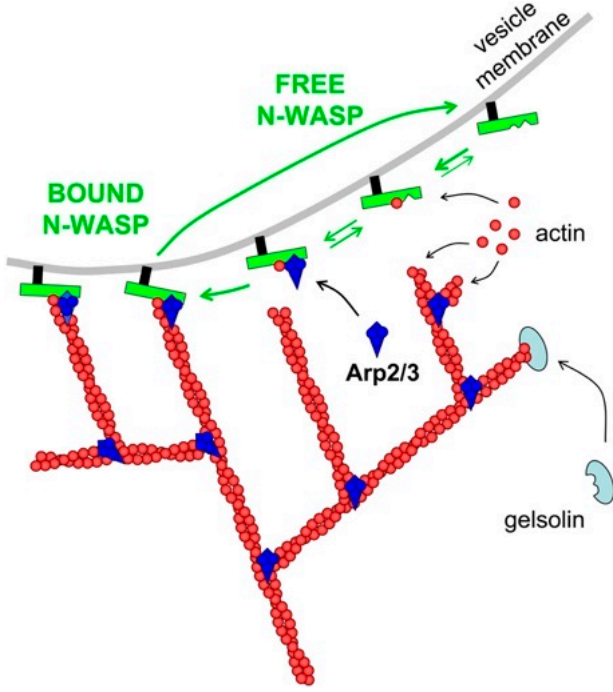


FIGURE 7 Relationship between the mobile states of N-WASP at the GUV surface and the elementary steps of filaments branching. N-WASP is anchored to the lipid membrane and binds G-actin in rapid equilibrium. N-WASP also binds the Arp2/3 complex. The ternary complex N-WASP-actin-Arp2/3 associates with the barbed end of an actin filament, tethering it to the membrane. Once G-actin and the Arp2/3 complex have detached from N-WASP, the branched junction allows the growth of a new branch in the actin network. Elongating actin filaments push against the membrane, and eventually get capped by gelsolin. The filament-bound and free states of N-WASP are featured. Note that the formation of the dendritic network tends to cluster N-WASP molecules by promoting the association of two individual N-WASP molecules to barbed ends branching off the same initial filament.

recorded in continuous movement was tested by a simple theoretical model, described as follows.

The point is to compute, at steady state, the surface density profile σ_b of N-WASP molecules that are bound to actin filaments (labeled b , for “bound”), and the profile σ_u of N-WASP molecules that are not bound (labeled u , for “unbound”). Unbound N-WASPs diffuse with a diffusion constant D , while bound N-WASPs are pulled toward the rear of the GUV with velocity v . N-WASP molecules switch between unbound and bound states with binding rate k_b and unbinding rate k_u , both expressed in s^{-1} . In principle, parameters D , v , k_b , and k_u can vary on the surface of the GUV. We will consider the GUV as spherical, with radius R , and the system as having a symmetry of revolution around the axis of movement. As a result, all parameters and densities depend on one spatial variable only, the arc length s , which varies from 0 at the rear of the GUV, to πR at the front.

At steady state, the following coupled differential equations must be satisfied,

$$\begin{cases} -\frac{\partial}{\partial s}[l(s)v(s)\sigma_b(s)] = [-\sigma_b(s)k_u(s) + \sigma_u(s)k_b(s)] \times l(s) \\ -\frac{\partial}{\partial s}\left[D(s)\frac{\partial}{\partial s}\sigma_u(s)\right] = [\sigma_b(s)k_u(s) - \sigma_u(s)k_b(s)] \times l(s) \end{cases} \quad (1)$$

where $l(s)$ is the length of the perimeter around the sphere at position s (i.e., the circle containing all points with the same value of s), $-v(s)\sigma_b(s)$ corresponds to the flux of bound N-WASPs, and $-D(s)(\partial/\partial s)\sigma_u(s)$ to the flux of unbound N-WASPs.

Similar drift-reaction differential equations have been written for similar situations, where objects alternate between a freely-diffusing state and an interacting state where they undergo directed movement (26,45). If $l(s)$ does not depend on s (e.g., the case where the object is a cylinder (45)), then it can be taken out of the expressions in Eq. 1. Here the object is a sphere, and $l(s) = 2\pi R \sin(s/R)$. However, we have checked that even in this case, $l(s)$ can be left out of the expressions in Eq. 1 without notably affecting the solution. The expressions in Eq. 1 are hence simplified, and become

$$\begin{cases} -\frac{\partial}{\partial s}[v(s)\sigma_b(s)] = -\sigma_b(s)k_u(s) + \sigma_u(s)k_b(s) \\ -\frac{\partial}{\partial s}\left[D(s)\frac{\partial}{\partial s}\sigma_u(s)\right] = \sigma_b(s)k_u(s) - \sigma_u(s)k_b(s) \end{cases}, \quad (2)$$

which is very similar to the equations used by Trichet et al. (26), with the notable difference that we here consider parameters D , v , k_u , and k_b as depending on the position s on the GUV. This is of primary importance, as we shall see.

Boundary conditions impose that the fluxes of bound and unbound N-WASP each be zero at $s = 0$ and at $s = \pi R$. At steady state, the sum of these two fluxes must be zero everywhere (for all s).

So an equivalent set of equations can be written:

$$\begin{cases} \frac{\partial}{\partial s}\left[D(s)\frac{\partial}{\partial s}\sigma_u(s)\right] = \frac{D(s)k_u(s)}{v(s)}\frac{\partial}{\partial s}\sigma_u(s) + k_b(s)\sigma_u(s) \\ \sigma_b(s) = -\frac{D(s)}{v(s)}\frac{\partial}{\partial s}\sigma_u(s) \end{cases} \quad (3)$$

Solving the first differential expression in Eq. 3 allows one to determine $\sigma_u(s)$, and $\sigma_b(s)$ can then be determined using the second equation.

This system cannot be solved analytically unless D , v , k_b , and k_u are all constants, in which case $\sigma_u(s)$ and $\sigma_b(s)$ are exponential functions (26), and the boundary conditions are not satisfied. We have used Euler’s method of function linearization to solve this system numerically. We are thus able, for any given values and variations of $D(s)$, $v(s)$, $k_b(s)$, and $k_u(s)$, analytical or not, to compute and plot the resulting surface densities for the bound and unbound populations of N-WASP molecules. We can then compare the resulting N-WASP density profile $\sigma_{N-WASP}(s) = \sigma_u(s) + \sigma_b(s)$ to the ones we have measured with fluorescent N-WASP.

N-WASP molecules that are bound to an actin filament are pulled toward the rear of the GUV, as the GUV moves with

velocity V_{GUV} with respect to the actin network. The bound N-WASP is pulled along a direction parallel to the axis of movement, but since it remains on the GUV surface, its displacement over a time dt is the projection of $V_{\text{GUV}} dt$ on the GUV surface (this corresponds to a minimal deformation of the actin network, to comply with the constraint that N-WASP remains on the GUV surface). Hence $v(s) = V_{\text{GUV}} \sin(s/R)$. This variation of $v(s)$ ensures that the boundary conditions are satisfied. For our computations, we have taken a typical V_{GUV} of $1 \mu\text{m}/\text{min}$.

Let us first consider the simplest model, where all the other parameters (D , k_b , and k_u) are constant. Based on published values (45,46) D is expected to be in the $1\text{--}10 \mu\text{m}^2/\text{s}$ range. The binding rate k_b is not known, and is assumed to increase with Arp2/3 concentration. The unbinding rate k_u is not known either, but a lower limit can be estimated, based on the following. Considering that filaments grow freely for an average time T_g and remain bound to the surface (via N-WASP)

for a time k_u^{-1} , the average distance L between two branching points is such that $L \cos(35^\circ) = V_{\text{GUV}} (k_u^{-1} + T_g)$ because of the average 35° angle between a filament and the normal to the surface. Since $T_g > 0$, this puts a lower limit on k_u . For a typical V_{GUV} of $1 \mu\text{m}/\text{min}$ and $L = 50 \text{ nm}$, this results in $k_u > 0.4 \text{ s}^{-1}$.

The resulting N-WASP density profiles are qualitatively similar to the ones we have measured experimentally. Comparing profiles computed for different values of k_b (Fig. 8 A), we see that lower values of k_b , corresponding to lower concentrations of Arp2/3, result in less segregated N-WASP profiles. For a given diffusion constant D (and keeping $k_u > 0.4 \text{ s}^{-1}$), the computed profiles depend only on the ratio k_b/k_u . For $D = 1 \mu\text{m}^2/\text{s}$ and $k_b/k_u = 3$, the segregation ratio is of the order of 0.6, in agreement with the measured value at 100 nM Arp2/3.

Compared to N-WASP, the VC domain interacts more weakly with the Arp2/3 complex, meaning that it should have a lower binding rate k_b and a higher unbinding rate k_u ,

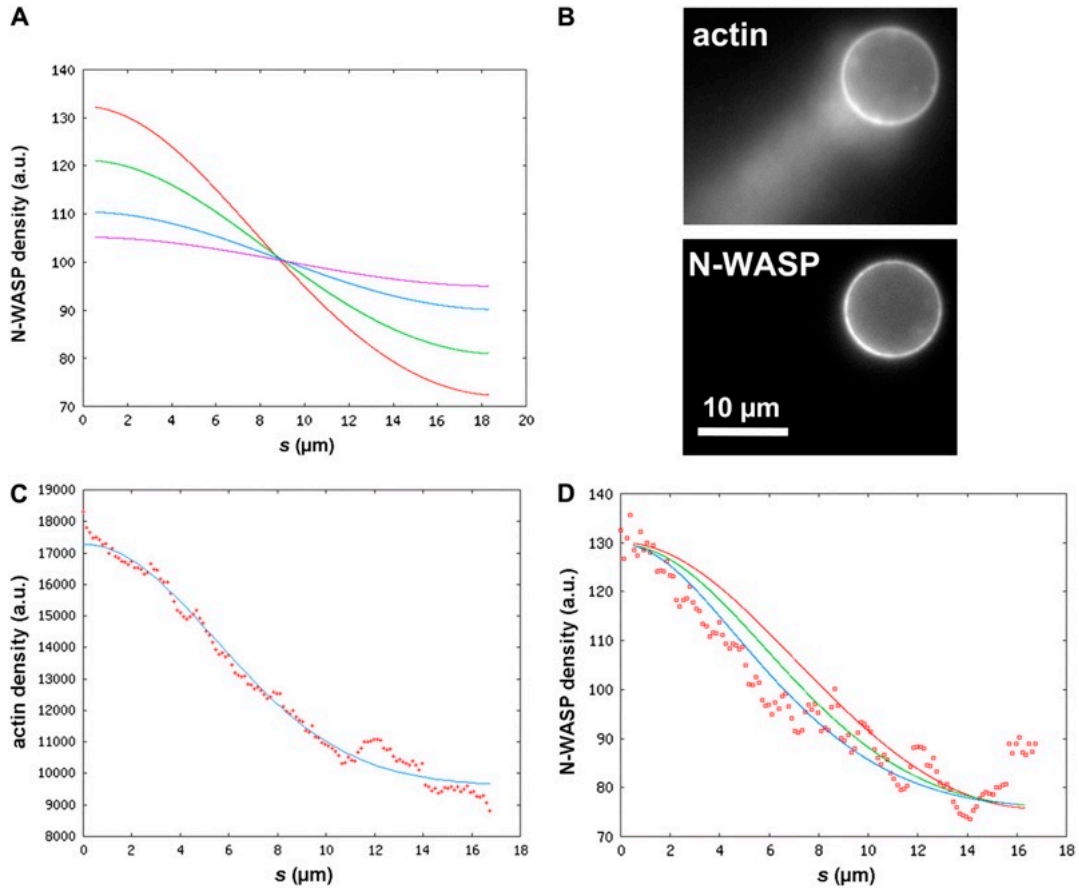


FIGURE 8 Computed N-WASP density profiles. (A) N-WASP density profiles computed with $V_{\text{GUV}} = 1 \mu\text{m}/\text{min}$, $D = 1 \mu\text{m}^2/\text{s}$, $k_u = 10 \text{ s}^{-1}$, and $k_b = 30 \text{ s}^{-1}$ (red curve), $k_b = 20 \text{ s}^{-1}$ (green curve), $k_b = 10 \text{ s}^{-1}$ (blue curve), and $k_b = 5 \text{ s}^{-1}$ (purple curve). The corresponding segregation ratios are 0.595, 0.565, 0.530, and 0.515, respectively. (B) Fluorescent actin and N-WASP from a $5.35 \mu\text{m}$ -radius GUV undergoing continuous movement. (C) Measured actin density profile along the vesicle shown in panel B (data points), fitted by the Gaussian function $f_{\text{act}}(s) = 0.442 \exp(-s^2/7.69^2) + 0.558$ (solid line). (D) Measured N-WASP density profile along the same vesicle (data points), compared to theoretical N-WASP profiles, computed with constant D , k_b and k_u (red curve, with $D = 1 \mu\text{m}^2/\text{s}$, $k_u = 1 \text{ s}^{-1}$, and $k_b = 3 \text{ s}^{-1}$); or taking the actin profile into account for $k_b(s)$ (green curve, with $D = 1 \mu\text{m}^2/\text{s}$, $k_u = 6 \text{ s}^{-1}$, $k_1 = 30 \text{ s}^{-1}$, and $k_2 = 20 \text{ s}^{-1}$), or taking the actin profile into account for $k_b(s)$ and $D(s)$ (blue curve, with $D_0 = 1.1 \mu\text{m}^2/\text{s}$, $a = 0.6$, $k_u = 2.25 \text{ s}^{-1}$, $k_1 = 20 \text{ s}^{-1}$, and $k_2 = 4 \text{ s}^{-1}$).

according to our model. This would lead to a higher proportion of unbound VC, with a low segregation ratio, and hereby a lower segregation ratio for the total VC population, in agreement with our observations (Fig. 5). VC-coated GUVs are nonetheless able to sustain continuous movement, probably due to differences in the mechanical properties of their actin filament network (e.g., a lower branching density), which are not included in this model. However, these properties are partly connected to the actin density profile (which is less segregated for VC- than for N-WASP-coated GUVs), which certainly has an impact on the nucleator density profile, and can be taken into account in our model, as explained in the following.

Including the actin filament density profile in the model

Using constant values of parameters D , k_u and k_b , and $k_u > 0.4 \text{ s}^{-1}$, the computed N-WASP density profiles are always symmetrical, with an inflection point located around $s = \pi R/2$ (Fig. 8 A). On the contrary, experimental N-WASP density profiles often have an inflection point positioned at smaller s -values, indicating that an important parameter controlling segregation has not been taken considered. In addition, the computed profiles of the two subpopulations of N-WASP have the same segregation ratio, whereas our experimental results, showing that Arp2/3 is more segregated than N-WASP, indicate that bound N-WASPs should be more segregated than free N-WASPs. This also indicates that the segregation of N-WASP is not driven solely by the pulling of bound N-WASPs.

The polarized distribution of actin filaments around the GUV should be considered, because it makes it more likely for N-WASP binding to take place at the rear of the GUV, and should enhance N-WASP segregation. In our model, this feature is expressed by the dependence of k_b on filament concentration. The binding of N-WASP to a filament is better described by a two-step process: the binding of Arp2/3, with rate k_1 proportional to Arp2/3 concentration, followed by the binding of an actin filament, with rate k_2 proportional to local actin filament concentration. The average lifetimes add up: $k_b^{-1}(s) = k_1^{-1} + k_2^{-1}(s)$, the s -dependence reflecting the local variations of actin filament density (we assume here that Arp2/3 concentration is homogeneous, though its diffusion could be locally limited by the density of the actin gel (47)). When the local actin density is high, it may also hinder the diffusion of free N-WASP molecules on the surface of the GUV, resulting in a varying diffusion coefficient $D(s)$.

Variations of local actin filament density are included in our model as follows. The actin density profile is measured (note that, in this model, the actin density profile is an experimentally determined parameter, and is not computed), and fitted with an arbitrary function (e.g., polynomial, Gaussian) We call $f_{\text{act}}(s)$ this function, after normalization of its maximum to 1. The rate constant for the binding of N-WASP-Arp2/3 to an actin filament is then written $k_2(s) = k_2 f_{\text{act}}(s)$.

As an example, the actin density profile around a $5.35 \mu\text{m}$ -radius GUV is well described by a Gaussian: $f_{\text{act}}(s) = 0.442 \exp(-s^2/7.69^2) + 0.558$ (Fig. 8, B–D). The computed profile, taking into account the effect of local actin density variations on k_b (through k_2 , as described earlier) is in better agreement with experimental data than the profile computed with a constant k_b (the inflection point is shifted toward lower values of s). In addition, a nonuniform k_b generates different segregation ratios for the two subpopulations of N-WASP molecules: bound N-WASPs are more segregated than free N-WASPs, in agreement with our observation that the Arp2/3 complex is more segregated than the (total) N-WASP population.

The description of our experimental data can be further improved by taking into account the effect of local actin filament concentration on the diffusion coefficient of N-WASP. Indeed, free N-WASP is expected to diffuse at a slower rate in regions where the density of filament-bound N-WASP is high (i.e., where the actin filament density is high). The following equation is proposed to account for the restrained diffusion of N-WASP: $D(s) = D_0 [1 - a f_{\text{act}}(s)]$, where D_0 corresponds to free, unhindered diffusion, and a is a constant that sets the amplitude of its limitation due to the presence of actin filaments. This is a very simple description, aiming at a qualitative evaluation of the impact of such an effect on the computed profiles (Fig. 7 D).

In conclusion, the computed profiles of N-WASP along the vesicle contour, based on a mechanism of interaction-driven segregation and diffusion, account for the main features of the corresponding experimental profiles. The model therefore validates our understanding of the molecular mechanism of actin-based motility and shows that the distribution of actin filaments around the GUV plays an important part in the segregation of N-WASP, and must be taken into account. This was not the case in a previously proposed description of the segregation-diffusion mechanism by Trichet et al. (26) where all parameters were considered constant. In the computations presented here, the actin density is considered as a fixed parameter that we determine from our experiments. However, the local density of actin filaments depends on the local frequency of branching, i.e., on local N-WASP density. As a development of the model presented here, numerical simulations seem better adapted to express the interdependence of actin and N-WASP densities. Simulations would also allow a better description of the two (or more) steps that lead to the binding of N-WASP to actin filaments.

SUPPLEMENTARY MATERIAL

We thank M.-A. Guedeau-Boudeville for osmometry measurements, D. Pantaloni and C. Le Clainche for guidance and discussions, and M. Bathe for his critical reading of the model section. G.R.L. also thanks S. Abbes for fruitful discussions on mathematics and numerical computation.

V.D. was supported by the Association pour la Recherche sur le Cancer. M.F.C. is supported in part by the Ligue Nationale Contre le Cancer (équipe labellisée), by the Agence Nationale de la Recherche (contract No. 06-PCVI-0011-01), and by a Human Frontier Science Program research grant No. RGP0072/2003-C. G.R.L. was supported by the European Specific Targeted Research Project “Active Biomics”.

REFERENCES

- Small, J. V., T. Stradal, E. Vignal, and K. Rottner. 2002. The lamellipodium: where motility begins. *Trends Cell Biol.* 12:112–120.
- Horwitz, A. R., and J. T. Parsons. 1999. Cell migration—movin’ on. *Science.* 286:1102–1103.
- Lauffenburger, D. A., and A. F. Horwitz. 1996. Cell migration: a physically integrated molecular process. *Cell.* 84:359–369.
- Small, J. V., M. Herzog, and K. Anderson. 1995. Actin filament organization in the fish keratocyte lamellipodium. *J. Cell Biol.* 129:1275–1286.
- Machesky, L. M., and R. H. Insall. 1999. Signaling to actin dynamics. *J. Cell Biol.* 146:267–272.
- Pollard, T. D., and G. G. Borisy. 2003. Cellular motility driven by assembly and disassembly of actin filaments. *Cell.* 112:453–465.
- Loisel, T. P., R. Boujemaa, D. Pantaloni, and M.-F. Carlier. 1999. Reconstitution of actin-based motility of *Listeria* and *Shigella* using pure proteins. *Nature.* 401:613–616.
- Bernheim-Groswasser, A., S. Wiesner, R. M. Golsteyn, M.-F. Carlier, and C. Sykes. 2002. The dynamics of actin-based motility depend on surface parameters. *Nature.* 417:308–311.
- Marcy, Y., J. Prost, M.-F. Carlier, and C. Sykes. 2004. Forces generated during actin-based propulsion: a direct measurement by micromanipulation. *Proc. Natl. Acad. Sci. USA.* 101:5992–5997.
- Pantaloni, D., C. Le Clainche, and M.-F. Carlier. 2001. Mechanism of actin-based motility. *Science.* 292:1502–1506.
- Wiesner, S., E. Helfer, D. Didry, G. Ducouret, F. Lafuma, M.-F. Carlier, and D. Pantaloni. 2003. A biomimetic motility assay provides insight into the mechanism of actin-based motility. *J. Cell Biol.* 160:387–398.
- Mogilner, A. 2006. On the edge: modeling protrusion. *Curr. Opin. Cell Biol.* 18:32–39.
- Marchand, J.-B., D. A. Kaiser, T. D. Pollard, and H. N. Higgs. 2001. Interaction of WASP/Scar proteins with actin and vertebrate Arp2/3 complex. *Nat. Cell Biol.* 3:76–82.
- Gerbal, F., V. Laurent, A. Ott, M. F. Carlier, P. Chaikin, and J. Prost. 2000. Measurement of the elasticity of the actin tail of *Listeria* monocytogenes. *Eur. Biophys. J.* 29:134–140.
- Iwasa, J. H., and R. D. Mullins. 2007. Spatial and temporal relationships between actin-filament nucleation, capping, and disassembly. *Curr. Biol.* 17:395–406.
- Co, C., D. T. Wong, S. Gierke, V. Chang, and J. Taunton. 2007. Mechanism of actin network attachment to moving membranes: barbed end capture by N-WASP WH2 domains. *Cell.* 128:901–913.
- Mogilner, A., and G. Oster. 2003. Force generation by actin polymerization II: the elastic ratchet and tethered filaments. *Biophys. J.* 84:1591–1605.
- Dickinson, R. B., and D. L. Purich. 2002. Clamped-filament elongation model for actin-based motors. *Biophys. J.* 82:605–617.
- Dickinson, R. B., and D. L. Purich. 2006. Diffusion rate limitations in actin-based propulsion of hard and deformable particles. *Biophys. J.* 91:1548–1563.
- Weisswange, I., T. Bretschneider, and K. I. Anderson. 2005. The leading edge is a lipid diffusion barrier. *J. Cell Sci.* 118:4375–4380.
- Giardini, P. A., D. A. Fletcher, and J. A. Theriot. 2003. Compression forces generated by actin comet tails on lipid vesicles. *Proc. Natl. Acad. Sci. USA.* 100:6493–6498.
- Delatour, V., S. Shekhar, A.-C. Reymann, D. Didry, K. H. D. Lê, G. Romet-Lemonne, E. Helfer, and M.-F. Carlier. 2008. Actin-based propulsion of functionalized hard versus fluid spherical objects. *N. J. Phys.* 10:025001.
- Heuvingh, J., M. Franco, P. Chavrier, and C. Sykes. 2007. ARF1-mediated actin polymerization produces movement of artificial vesicles. *Proc. Natl. Acad. Sci. USA.* 104:16928–16933.
- Upadhyaya, A., J. R. Chabot, A. Andreeva, A. Samadani, and A. van Oudenaarden. 2003. Probing polymerization forces by using actin-propelled lipid vesicles. *Proc. Natl. Acad. Sci. USA.* 100:4521–4526.
- Boukellal, H., O. Campas, J. F. Joanny, J. Prost, and C. Sykes. 2004. Soft *Listeria*: actin-based propulsion of liquid drops. *Phys. Rev. E Stat. Nonlin. Soft Matter Phys.* 69:061906.
- Trichet, L., O. Campas, C. Sykes, and J. Plastino. 2007. VASP governs actin dynamics by modulating filament anchoring. *Biophys. J.* 92:1081–1089.
- Mathivet, L., S. Cribier, and P. F. Devaux. 1996. Shape change and physical properties of giant phospholipid vesicles prepared in the presence of an AC electric field. *Biophys. J.* 70:1112–1121.
- Spudich, J. A., and S. Watt. 1971. The regulation of rabbit skeletal muscle contraction. I. Biochemical studies of the interaction of the tropomyosin-troponin complex with actin and the proteolytic fragments of myosin. *J. Biol. Chem.* 246:4866–4871.
- Isambert, H., P. Venier, A. C. Maggs, A. Fattoum, R. Kassab, D. Pantaloni, and M. F. Carlier. 1995. Flexibility of actin filaments derived from thermal fluctuations. Effect of bound nucleotide, phalloidin, and muscle regulatory proteins. *J. Biol. Chem.* 270:11437–11444.
- Pantaloni, D., R. Boujemaa, D. Didry, P. Gounon, and M. F. Carlier. 2000. The Arp2/3 complex branches filament barbed ends: functional antagonism with capping proteins. *Nat. Cell Biol.* 2:385–391.
- Gutsche-Perelroizen, I., J. Lepault, A. Ott, and M. F. Carlier. 1999. Filament assembly from profilin-actin. *J. Biol. Chem.* 274:6234–6243.
- Egile, C., T. P. Loisel, V. Laurent, R. Li, D. Pantaloni, P. J. Sansonetti, and M. F. Carlier. 1999. Activation of the CDC42 effector N-WASP by the *Shigella flexneri* IcsA protein promotes actin nucleation by Arp2/3 complex and bacterial actin-based motility. *J. Cell Biol.* 146:1319–1332.
- Grabarek, Z., and J. Gergely. 1990. Zero-length crosslinking procedure with the use of active esters. *Anal. Biochem.* 185:131–135.
- Le Clainche, C., D. Didry, M. F. Carlier, and D. Pantaloni. 2001. Activation of Arp2/3 complex by Wiskott-Aldrich Syndrome protein is linked to enhanced binding of ATP to Arp2. *J. Biol. Chem.* 276:46689–46692.
- Lee, E., and D. A. Knecht. 2002. Visualization of actin dynamics during macropinocytosis and exocytosis. *Traffic.* 3:186–192.
- Merrifield, C. J., U. Rescher, W. Almers, J. Proust, V. Gerke, A. S. Sechi, and S. E. Moss. 2001. Annexin 2 has an essential role in actin-based macropinocytic rocketing. *Curr. Biol.* 11:1136–1141.
- Bernheim-Groswasser, A., J. Prost, and C. Sykes. 2005. Mechanism of actin-based motility: a dynamic state diagram. *Biophys. J.* 89:1411–1419.
- Lasa, I., E. Gouin, M. Goethals, K. Vancompernelle, V. David, J. Vandekerckhove, and P. Cossart. 1997. Identification of two regions in the N-terminal domain of ActA involved in the actin comet tail formation by *Listeria* monocytogenes. *EMBO J.* 16:1531–1540.
- Rafelski, S. M., and J. A. Theriot. 2005. Bacterial shape and ActA distribution affect initiation of *Listeria* monocytogenes actin-based motility. *Biophys. J.* 89:2146–2158.
- Bosch, M., K. H. Le, B. Bugyi, J. J. Correia, L. Renault, and M. F. Carlier. 2007. Analysis of the function of Spire in actin assembly and its synergy with formin and profilin. *Mol. Cell.* 28:555–568.
- Chereau, D., F. Kerff, P. Graceffa, Z. Grabarek, K. Langsetmo, and R. Dominguez. 2005. Actin-bound structures of Wiskott-Aldrich syn-

- drome protein (WASP)-homology domain 2 and the implications for filament assembly. *Proc. Natl. Acad. Sci. USA*. 102:16644–16649.
42. Hertzog, M., C. van Heijenoort, D. Didry, M. Gaudier, J. Coutant, B. Gigant, G. Didelot, T. Preat, M. Knossow, E. Guittet, and M. F. Carlier. 2004. The β -thymosin/WH2 domain; structural basis for the switch from inhibition to promotion of actin assembly. *Cell*. 117: 611–623.
 43. McGrath, J. L., N. J. Eungdamrong, C. I. Fisher, F. Peng, L. Mahadevan, T. J. Mitchison, and S. C. Kuo. 2003. The force-velocity relationship for the actin-based motility of *Listeria monocytogenes*. *Curr. Biol*. 13:329–332.
 44. Alberts, J. B., and G. M. Odell. 2004. In silico reconstitution of *Listeria* propulsion exhibits nano-saltation. *PLoS Biol*. 2:e412.
 45. Leduc, C., O. Campas, K. B. Zeldovich, A. Roux, P. Jolimaitre, L. Bourel-Bonnet, B. Goud, J.-F. Joanny, P. Bassereau, and J. Prost. 2004. Cooperative extraction of membrane nanotubes by molecular motors. *Proc. Natl. Acad. Sci. USA*. 101:17096–17101.
 46. Sprague, B. L., and J. G. McNally. 2005. FRAP analysis of binding: proper and fitting. *Trends Cell Biol*. 15:84–91.
 47. Plastino, J., I. Lelidis, J. Prost, and C. Sykes. 2004. The effect of diffusion, depolymerization and nucleation promoting factors on actin gel growth. *Eur. Biophys. J*. 33:310–320.